

Supporting information for the manuscript "Using large-eddy simulations with explicit aerosol-cloud interactions to understand observed effects of Secondary Ice Production in summer cumulus clouds"

S1 Instrumentation used in the SPICULE-RF04b flights

Table S1. List of parameters and instrumentation relevant to this study and related to the characterization of the SPICULE-RF04b cloud case on June 05, 2021 (Lawson et al., 2023; Heymsfield et al., 2024)

Parameter	Instrument	Flight
Temperature	Rosemount Model 102 and 510BH	Learjet, GV
Altitude	Royal Air FAA RVSM Certification	Learjet, GV
Horizontal and vertical wind components	Aventech AIMMS - 20	Learjet, GV
Dew point temperature	EdgeTech Chilled Mirror 137	Learjet, GV
Liquid water, total water	Sky Tech Nevzorov LWC/TWC	Learjet, GV
Cloud droplets (2-50 μ m)	SPEC Fast Forward Scattering Spectrometer Probe (FFSSP)	Learjet, GV
Cloud droplets (2-50 μ m)	SPEC Fast Cloud Droplet Probe (FCDP)	Learjet, GV
Cloud particles (10 μ m-3mm)	SPEC 2D-S (stereo) optical array spectrometer	Learjet, GV
Cloud particles (2-50 μ m)	SPEC Hawkeye-FCDP	Learjet, GV
Cloud particles (10 μ m-3mm)	SPEC Haweye-2DS	Learjet, GV
Precipitation droplets (150 μ m-2cm)	SPEC High Volume Precipitation Spectrometer (HVPS-3)	Learjet, GV
Cloud particle habit, high resolution imagery	SPEC Hawkeye-CPI	GV
	Digital holographic particle imager (HOLODEC)	GV
Immersion freezing temperature spectra	Colorado State University Ice Spectrometer (IS)	GV
Giant Cloud Condensation Nuclei (CCN) (0.7-20 μ m)	NCAR/EOL/RAF Giant Cloud Condensation Nuclei Impactor (GNI)	GV
Aerosol concentration (10 nm - 3 μ m)	TSI Water-based Condensation Particle Counter (CPC)	GV
Aerosol concentration (100 nm - 3 μ m)	DMT Passive Cavity Aerosol Spectrometer (PCASP)	GV
Reflectivity, spectral width, and velocity	ProSensing 35.6 GHz Ka-band probe radar	Learjet
Doppler radial velocity	HIAPER Cloud Radar (HCR)	GV

5 S2 Parameterizations of SIP rates in UCLALES-SALSA

In this study, SIP rates describing the number concentration of secondary ice particles generated by a SIP mechanism in a period of time dN_i/dt are calculated as

$$\left. \frac{dN_i}{dt} \right|_{\text{SIP}} = \sum_{D_{m,\min}}^{D_{m,\max}} \sum_{D_{l,\min}}^{D_{l,\max}} N_{\text{SIP}}(T, D_l, D_m) = \sum_{D_{m,\min}}^{D_{m,\max}} \sum_{D_{l,\min}}^{D_{l,\max}} \text{IMF}(T, D_l, D_m) J(D_l, D_m), \quad (\text{Eq.S1})$$

$$\left. \frac{dN_i}{dt} \right|_{\text{SIP}} = \sum_{D_{m,\min}}^{D_{m,\max}} \sum_{D_{l,\min}}^{D_{l,\max}} \text{IMF}(T, D_l, D_m) J(D_l, D_m), \quad (\text{Eq.S2})$$

- 10 where D_l and D_m represent the size of interacting hydrometeors l and m , T is the air temperature, $N_{\text{SIP}}(T, D_l, D_m)$ is the number concentration of secondary ice particles generated by a SIP event between the selected hydrometeors. This variable can be expressed in terms of the product between the ice multiplication factor $\text{IMF}(T, D_l, D_m)$ or number of secondary ice

fragments generated per SIP event; and the term $J(D_l, D_m) dD_l dD_m$ is the frequency of occurrence of SIP events per unit of time per unit volume. Sum operators are carried out along size bins of hydrometeor types involved in the SIP mechanism.

15 The conceptual SIP modelling framework in Eq. (Eq.S2) indicates general dependencies on air temperature T and hydrometeor size D , however calculations of IMF and conditional collision kernels include a multiplicity of implicit dependencies that are intrinsic to each SIP mechanism (e.g. rime fraction dependency of the size, density, velocity of ice particles). Equation (Eq.S2) can be expressed as the sum of several similar terms, one per each SIP mechanism acting on the cloud domain. SIP rates vary temporally and spatially but we have omitted here these dependencies just to simplify the representation.

20 The ice multiplication factor IMF (T, D_l, D_m) is calculated from parametrizations as the product of two terms, the term $g(D_l, D_m)$ to account for the relative size of interacting hydrometeors and the term $h(T)$ to account for temperature effects as follows

$$\text{IMF}(T, D_l, D_m) = g(D_l, D_m) h(T). \quad (\text{Eq.S3})$$

The occurrence of SIP events is calculated using a conditional gravitational collision kernel expressed as

$$25 \quad J(D_l, D_m) = \mathcal{E}(D_l, D_m) K(D_l, D_m) N_l(D_l) N_m(D_m), \quad (\text{Eq.S4})$$

where $\mathcal{E}(D_l, D_m)$ is a binary variable that changes from 0 to 1 if the relative size triggering conditions are satisfied, $K(D_l, D_m)$ is the gravitational collision kernel based on the actual cross section of the colliding hydrometeors, $N_l(D_l)$ and $N_m(D_m)$ are the binned number concentrations of hydrometeors type l and type m (e.g. precipitation droplet and ice particle). The collision kernel calculation includes the sticking efficiency if SIP events correspond to ice–ice collisions. This efficiency is inversely proportional to the fraction of rime ice and varies between 30% and 0.05% for fractions between 0 and 1 (?).

30 UCLALES-SALSA has implemented parameterizations for three mechanisms of secondary ice production, rime splintering (RS), droplet shattering (DS) and ice–ice collisional break up (IIBR). Table S2 summarizes parameterizations implemented in UCLALES–SALSA to model ice multiplication factors in Eq.S2 using Eq.S3. The size distribution of secondary ice particles is explained in the main paper.

Table S2. Parametrization for ice multiplication factors due to secondary ice production through the mechanisms of rime splintering (RS), droplet shattering (DS) and ice–ice collisional breakup (IIBR).

SIP mechanism	IMF as in (Eq.S3)	
	$g(D_d, D_i)$	$h(T)$
RS	Hallet and Mossop (1974) Mossop (1976)	Cotton et al. (1986) Ziegler et al. (1986) Ferrier (1994) Sullivan et al. (2018)
DS	Lawson et al. (2015) Lawson et al. (2015) Mode 1 or simple in Phillips et al. (2018) Mode 2 or full in Phillips et al. (2018)	Unrestricted Sullivan et al. (2018) based on Leisner et al. (2014) Phillips et al. (2018) Phillips et al. (2018)
IIBR	Takahashi et al. (1995) Phillips et al. (2017) modified by Grzegorzczak et al. (2025) Takahashi et al. (1995)	Sullivan et al. (2017) Phillips et al. (2017) Sotiropoulou et al. (2021)

35 The expression for the ice multiplication factor (IMF) in the parameterization of Phillips et al. (2017) was corrected by Grzegorzczak et al. (2025) based on replicates of the Takahashi et al. (1995) experiments (Grzegorzczak et al., 2023). However, the new model parameters reported in Table 2 of Grzegorzczak et al. (2025) were mistyped and a corrected version of them was kindly provided by the author in a personal communication. The correct expressions for the variable A_M or number density (per unit area) of breakable vapor-grown branches or other asperities on the colliding surfaces in the region of contact and C

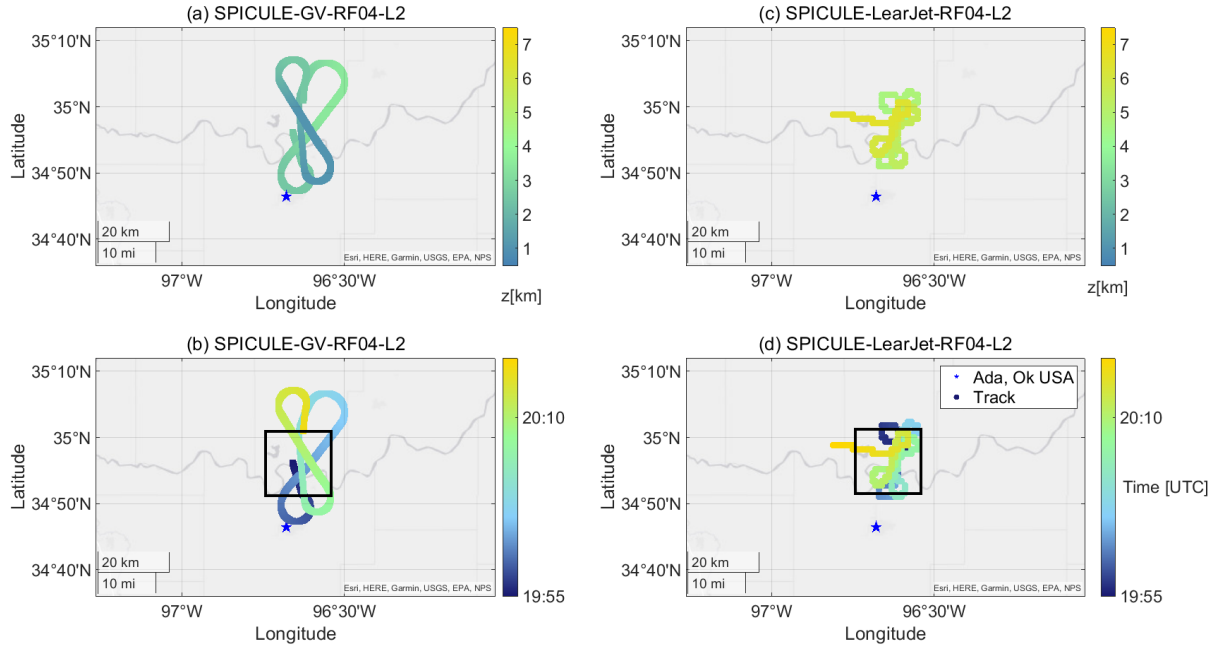


Figure S1. Temporal variation in the altitude of research flights during the SPICULE-RF04b cloud case of 05 June 2021 compared to the size of the model domain (black square). Panels (a-b): GV-flight. Panels (c-d): Learjet-flight

- 40 the asperity-fragility coefficient for rimed ice particles are shown in (Eq.S5) and (Eq.S6). At the same temperature and relative hydrometeor size conditions, ice multiplication factors from the Phillips-Grzegorzczuk's parameterization are lower than those from the parametrization of Sotiropoulou et al. (2021) when the rime fraction is below 0.5, but substantially higher above this threshold with a better agreement to the experimental values reported by Takahashi et al. (1995).

$$A_M [m^{-2}] = \exp(14.74S_i + 14.28) \quad (\text{Eq.S5})$$

45 $C[J^{-1}] = \exp(20.15S_i + 13.78) \quad (\text{Eq.S6})$

S3 Flight tracks and model domain size

- Simulations were performed in a model domain of 28.8 km x 28.8 km x 12 km with horizontal and vertical resolution of 300 m and 60 m respectively. The model domain size was selected based on the surface area covered simultaneously by the GV and Learjet flights on 05 June 2021 (UCAR/NCAR - Earth Observing Laboratory, 2021). This time interval coincides with the
- 50 early stage of the cloud system in which ice multiplication was observed in the rising cloud tower.

S4 Ice nucleating abilities of aerosol particles

Rates of ice formation via immersion freezing are calculated with the parameterization of Savre et al. (2014) that calculates the distribution of the freezing probability an aerosol population using a time evolving contact angle distribution (Tonttila

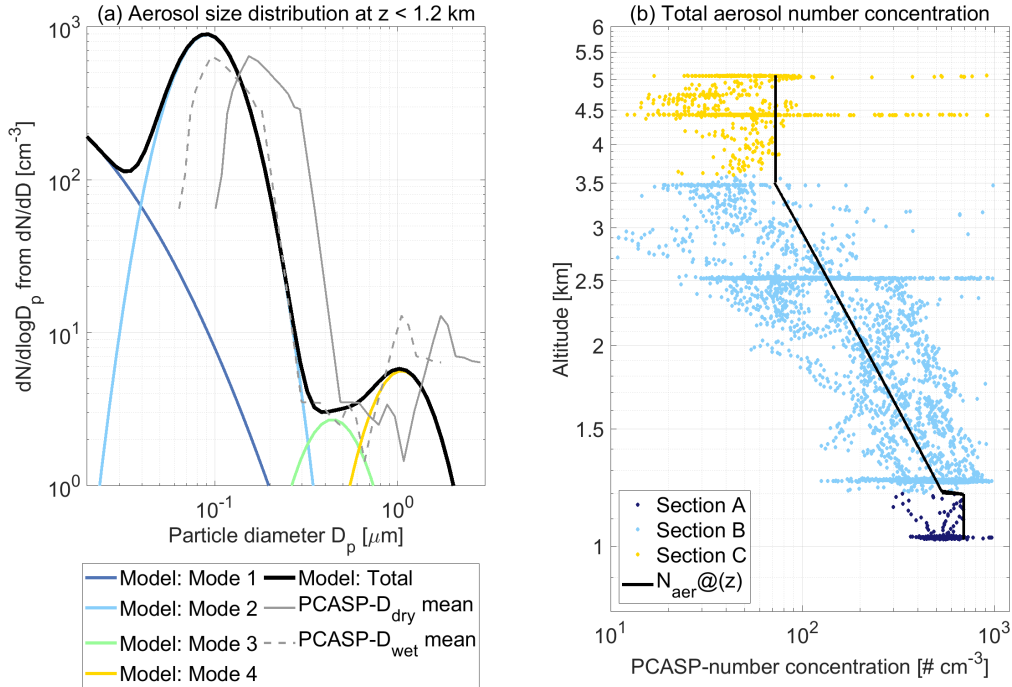


Figure S2. Aerosol properties used for model initialization in the SIP-OFF and SIP-ON simulation scenarios (a) Multimodal lognormal size distribution used for model initialization (black line) compared to PCASP-dry (dashed grey) and PCASP-wet (continuous gray) particle size distributions observed below 1.2 km during the SPICULE-RF04b-GV flight. The dry particle size was estimated by inverting with a κ equal to . (b) Vertical profile of total aerosol number concentrations (black line) based on PCASP measurements during the SPICULE-RF04b-GV flight.

et al., 2021). In principle if SIP processes are turned off, modeled ice number concentrations corresponding to updraft-cloudy conditions with low fraction of rimed ice should be representative of fresh pristine ice particles. Figure S3 represents the mean values of ice number concentrations modeled in the SIP-OFF scenario. Modeled cloud microphysics were sampled for cloudy updrafts and compared them with number concentrations of ice nucleating particles observed during the SPICULE-RF04b-GV flight (DeMott et al., 2024) and those given by the parameterization of Fletcher (1969). We can notice a relatively good agreement at temperatures between $-16\text{ }^{\circ}\text{C}$ and $-14\text{ }^{\circ}\text{C}$ suggesting that our assumptions about the contact angle distribution were adequate. The positive deviations of modeled ice number concentrations at warmer temperatures correspond to grid points where ice was present due to sedimentation from upper colder sections. We did not apply any correction to avoid this specific situation.

S5 Model sensitivity analysis

We performed a sensitivity analysis to determine changes in cloud dynamics induced by variations in the aerosol loading and the convection intensity. We modified the atmospheric soundings and aerosol properties used for model initialization to find the model setup with the closest agreement between modeled and observed microphysics at the uppermost cloud section. The potential temperature in the well-mixed layer as well as the specific humidity and temperature at high altitudes in the atmospheric soundings was modified to test three different convection intensity levels, here referred to as CAPE-low, CAPE-mid and CAPE-hi. Figure S4 depicts the skew-TP diagrams corresponding to the different sounding profiles. We also compared

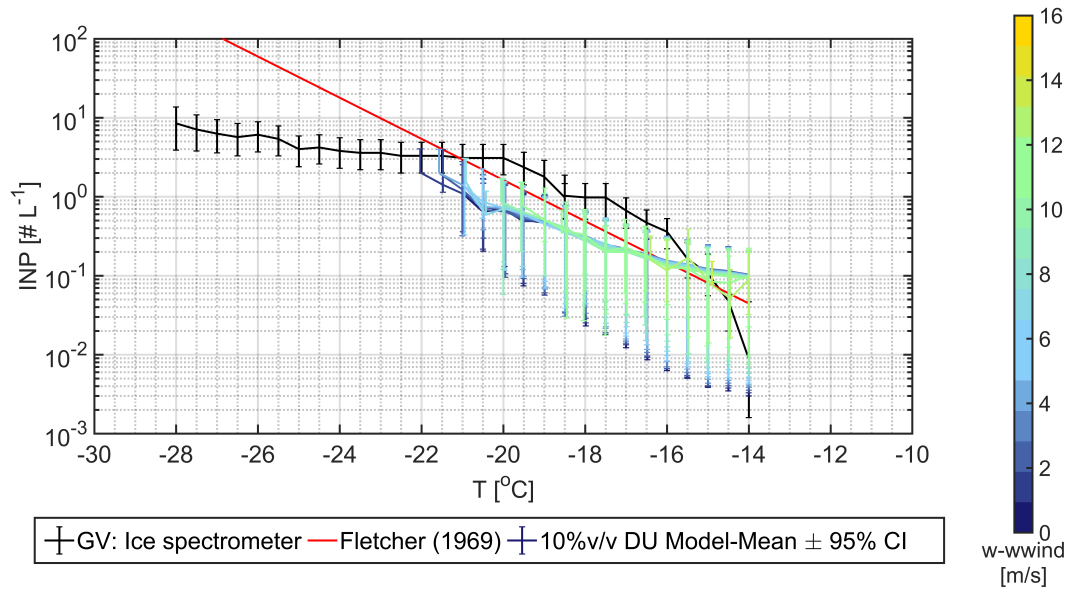


Figure S3. Temperature-dependence of number concentrations for ice nucleating particles observed by the GV-Ice spectrometer and calculated with the parametrization of Fletcher (1969) compared to ice number concentrations in the SIP-OFF scenario.

- 70 simulations initialized with different aerosol number concentration in the accumulation mode (i.e. mean dry diameter of 100 nm) while mean dry diameters and variance of the remaining particle modes were kept constant. In this way we investigated possible mixed-phase invigoration effects caused by increasing fine particle concentrations (Fan et al., 2022). The aerosol levels are referred to A-low and A-hi respectively. As the convective available potential energy (CAPE) which is closely linked to the level of neutral buoyancy (LNB), our sensitivity analysis also assessed possible changes in cloud top conditions due to higher
- 75 LNB values. The different simulation scenarios are described in Table S3.

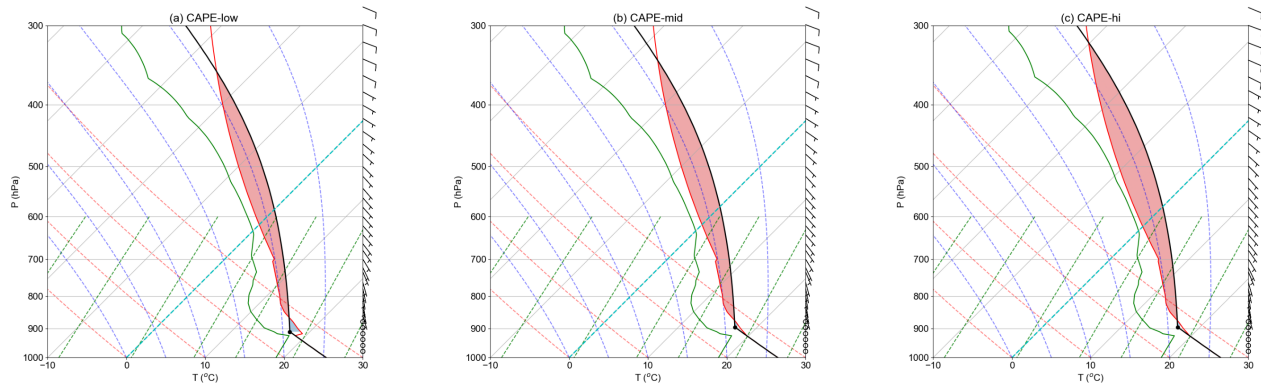


Figure S4. Vertical profile of atmospheric variables in an skew T-logP diagram including temperature (red) and dew point temperature (green) profiles as well as the CAPE (red shaded area) and lifting condensation level (LCL, black dot) used for model initialization in the simulation scenarios (a) CAPE-low or C_low (b) CAPE-mid or C_mid (c) CAPE-hi or C_hi

Table S3. Simulation scenarios with input variables and parametrizations selected related to model tuning

Scenario	LCL [hPa, °C]	EL [hPa, °C]	CAPE [Jkg ⁻¹]	Accum. mode [mg ⁻¹]	SIP - DS	SIP – IIBR
C_low-A_low-SIP_S	910.6 17.5	354.5 -24.8	487.2	616	Phillips et al. (2018)	Sotiropoulou et al. (2021)
C_mid-A_low-SIP_S	895.4 17.2	340.5 -26.5	611.3	616	Phillips et al. (2018)	Sotiropoulou et al. (2021)
C_mid-A_hi-SIP_S	895.4 17.2	340.5 -26.5	611.3	810	Phillips et al. (2018)	Sotiropoulou et al. (2021)
C_hi_A_hi_PIP	895.4 17.2	318.9 -30.3	763.7	810	OFF	OFF
C_hi_A_hi_SIP_S	895.4 17.2	318.9 -30.3	763.7	810	Phillips et al. (2018)	Sotiropoulou et al. (2021)
C_hi_A_hi_SIP_P	895.4 17.15	318.9 -30.3	763.7	810	Phillips et al. (2018)	Phillips et al. (2017) modified by Grzegorz et al. (2025)

We summarize here the research findings leading to the selection of the optimal model setup:

1. Decreasing potential temperature at the well-mixed layer: colder conditions at the well-mixed layer produce weaker convection, lower CAPE. Despite the good agreement between observed and modeled LWC values below 2.5 km, with lower CAPE, there was no significant ice formation about the freezing level.
- 80 2. Increasing the aerosol accumulation mode: from step 1, we kept the case with a warmer well-mixed layer (i.e. stronger CAPE) but now ran the simulation with higher aerosol loading. Droplet activation rate increased leading to smaller droplets that suppressed drizzle formation. This allowed more cloud water to be lifted above, favoring in-cloud activation which in turn intensified convection to lift more cloud water up above the freezing level (approx. 4 km). With more ice, ice deposition and riming rates were also higher, particularly above 5.5 km where temperature decreased below -8.5 °C(max. Wegener-Bergeron-Findeisen WBF process). Latent heat released due to mixed phase processes, invigorated convection, and the cloud top rose showing ice at higher altitudes but not enough to reach the observed levels.
- 85 3. Increasing CAPE and decreasing LNB pressure: from step 2, we kept the higher aerosol loading but increased the CAPE moving the sounding towards colder temperatures above 3 km (no changes below this level). There were no significant changes in the agreement between modeled and observed droplet size distribution, but with a stronger CAPE updrafts became stronger producing a significant increment in cloud liquid water in the middle and upper cloud sections. Modeled and observed droplet size distributions now agreed well at both below and above freezing levels. With more convective energy, our simulation showed an increment in the water-phase partitioning (more cloudy spots with liquid) which in turn translated into higher ice number concentrations and SIP rates. With more cloud liquid water, all ice processes were enhanced via warm and cold phase invigoration leading to a better agreement between observed and modeled values at the colder temperature levels, especially at -17.65 °C.
- 90 4. Turning off SIP processes: from step 4 we kept all model settings but switched off SIP processes. Ice formation occurred just by primary ice formation (PIP) via immersion freezing. Without SIP, there were significant changes in the LWC vertical profile with significantly lower values above freezing level. Ice number concentrations decreased up to two
- 95

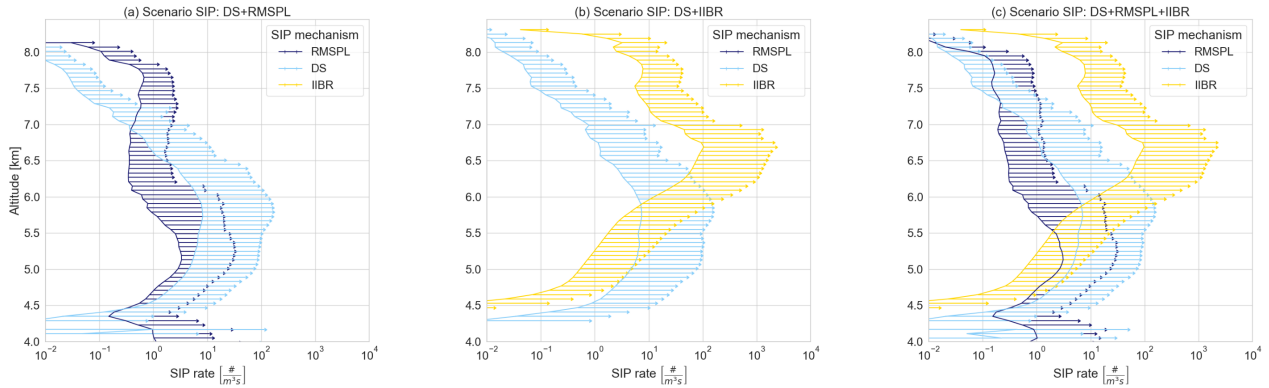


Figure S5. Horizontal averages of SIP rates due to rime splintering (SIP-RS), droplet shattering (SIP-DS), ice-ice collisional breakup (SIP-IIBR) in different simulation scenarios. The simulation accounted for secondary ice production by (a) SIP-RS and SIP-DS, (b) SIP-DS and SIP-IIBR (c) SIP-RS, SIP-DS and SIP-IIBR. Colored arrows go from the mean to the mean plus the standard deviation. Mean values were obtained by averaging SIP rates in cloudy points along the simulation time of two hours.

orders of magnitude indicating that mixed-phase invigoration related to ice processes above freezing level was essential to reproduce observed cloud dynamics and microphysics.

We also performed a sensitivity analysis running simulation scenarios with high levels of CAPE and aerosol loading during model initialization (i.e. scenario C_hi_A_hi), but using different combinations of SIP mechanisms, (a) rime splintering and droplet shattering, (b) droplet shattering and ice-ice collisional breakup and (c) all three SIP mechanisms considered in this study. For the sake of simplicity we have included in Figure S5 vertical profiles of SIP rates per mechanism calculated as horizontal averages in cloudy points along the simulation time. When simulations included just SIP mechanisms involving supercooled droplets that is rime splintering and droplet shattering, Figure S5(a), rates of secondary ice were not high enough to reproduce observed ice microphysics, the SIP-DS mechanism dominated the lower part of the cold cloud section, while the SIP-RS was active at the upper part likely due to smaller sizes of supercooled droplets (i.e. SIP-RS involves droplets with diameter larger than 24 μm). Due to the dominant role of the SIP-DS, we combined it with SIP-IIBR and found a positive-feedback that boosted the ice multiplication phenomena and gave a good representation of ice microphysics. Figure S5(a) shows how SIP-DS increased in the upper cold section compared to the those in the SIP-RS-DS scenario, and decreased slightly at altitudes where both mechanisms had comparable rates. When all three SIP mechanisms were combined (i.e. SIP-ON scenario discussed in the main text), the symbiotic relationship between SIP-DS and SIP-IIBR was preserved and the SIP-RS caused very modest reduction in rates of SIP-DS at the lower part of the cold cloud section.

S6 Additional supporting figures

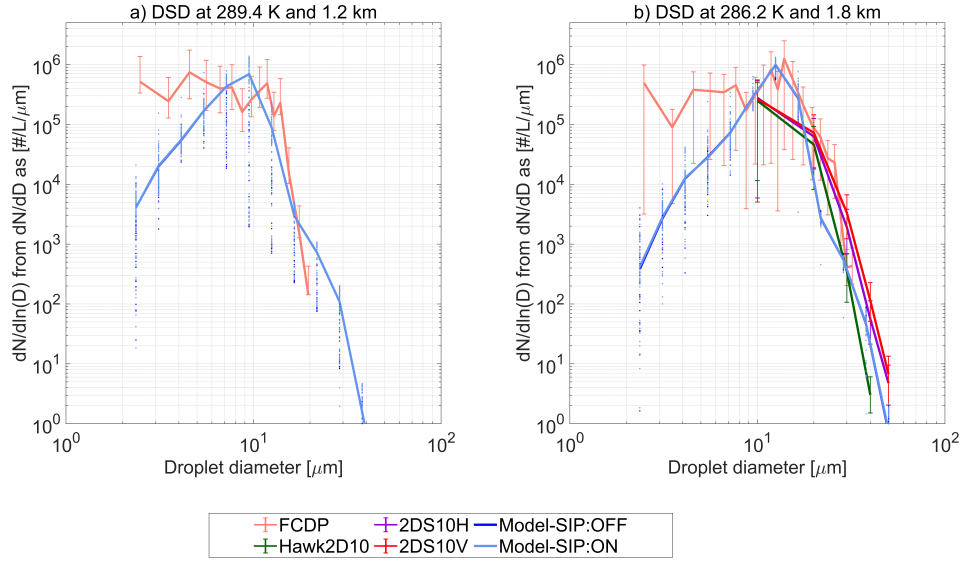


Figure S6. Droplet size distributions in updrafts at the lower part of the warm cloud section (a) 1.4 km (b) 1.8 km. Observations are shown as mean values with error bars going from the 50th to the 99th percentile and labeled according to the nomenclature described in Table S-1. Modeled values are shown as mean horizontal values with dotted lines along size bins indicating variability across cloudy points with LWC > 0.01 gm⁻³ and updraft velocity > 0.02 ms⁻¹.

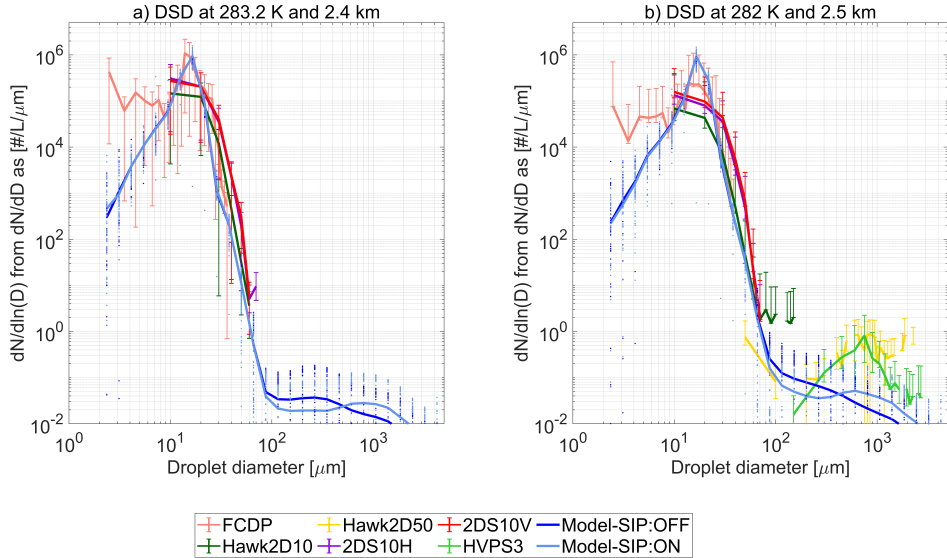


Figure S7. Droplet size distributions in updrafts at the mid part of the warm cloud section (a) 2.3 km (b) 2.5 km. Observations are shown as mean values with error bars going from the 50th to the 99th percentile and labeled according to the nomenclature described in Table S-1. Modeled values are shown as mean horizontal values with dotted lines along size bins indicating variability across cloudy points with LWC > 0.01 gm⁻³ and updraft velocity > 0.02 ms⁻¹.

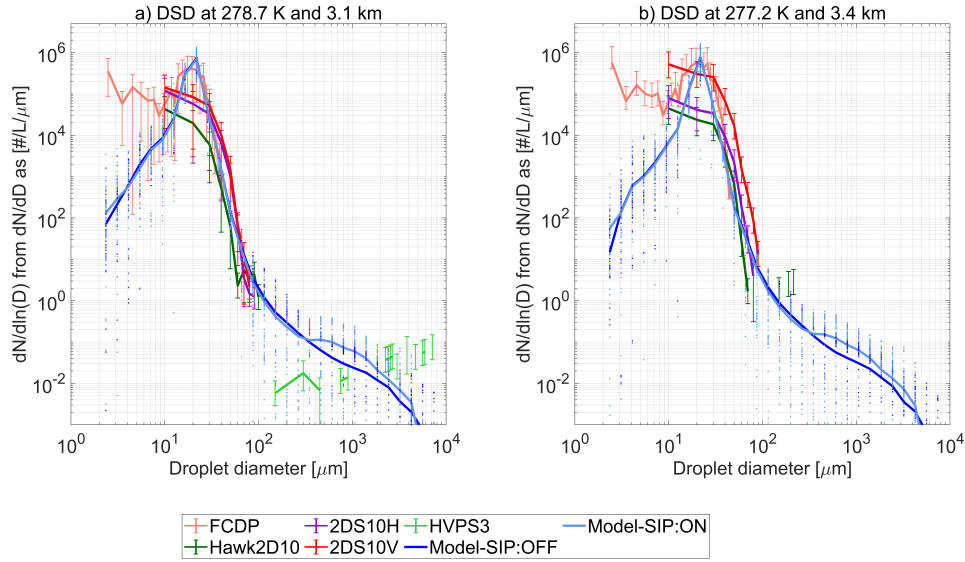


Figure S8. Droplet size distributions in updrafts at the upper part of the warm cloud section (a) 3.1 km (b) 3.4 km. Observations are shown as mean values with error bars going from the 50th to the 99th percentile and labeled according to the nomenclature described in Table S-1. Modeled values are shown as mean horizontal values with dotted lines along size bins indicating variability across cloudy points with LWC > 0.01 gm⁻³ and updraft velocity > 0.02 ms⁻¹.

References

- Cotton, W. R., Tripoli, G. J., Rauber, R. M., and Mulvihill, E. A.: Numerical Simulation of the Effects of Varying Ice Crystal Nucleation Rates and Aggregation Processes on Orographic Snowfall, *Journal of Applied Meteorology and Climatology*, 25, 1658–1680, [https://doi.org/10.1175/1520-0450\(1986\)025<1658:NSOTEO>2.0.CO;2](https://doi.org/10.1175/1520-0450(1986)025<1658:NSOTEO>2.0.CO;2), 1986.
- 120 DeMott, P., Hill, T., and Patnaude, R.: SPICULE: CSU Ice Spectrometer (IS) Measurements. Version 1.0, <https://doi.org/10.26023/HAYW-8STD-KT00>, accessed 09 Jun 2025, 2024.
- Fan, J., Li, Z., and (ed.), K. S. C.: Chapter 14 - Aerosol interactions with deep convective clouds, pp. 571–617, Elsevier, <https://doi.org/10.1016/B978-0-12-819766-0.00001-8>, 2022.
- Ferrier, B. S.: A Double-Moment Multiple-Phase Four-Class Bulk Ice Scheme. Part I: Description, *Journal of Atmospheric Sciences*, 51, 249 – 280, [https://doi.org/10.1175/1520-0469\(1994\)051<0249:ADMMPF>2.0.CO;2](https://doi.org/10.1175/1520-0469(1994)051<0249:ADMMPF>2.0.CO;2), 1994.
- 125 Fletcher, N. H.: Active Sites and Ice Crystal Nucleation, *Journal of Atmospheric Sciences*, 26, 1266 – 1271, [https://doi.org/10.1175/1520-0469\(1969\)026<1266:ASAICN>2.0.CO;2](https://doi.org/10.1175/1520-0469(1969)026<1266:ASAICN>2.0.CO;2), 1969.
- Grzegorzczuk, P., Yadav, S., Zanger, F., Theis, A., Mitra, S. K., Borrmann, S., and Szakáll, M.: Fragmentation of ice particles: laboratory experiments on graupel–graupel and graupel–snowflake collisions, *Atmospheric Chemistry and Physics*, 23, 13 505–13 521, <https://doi.org/10.5194/acp-23-13505-2023>, 2023.
- 130 Grzegorzczuk, P., Wobrock, W., Canzi, A., Niquet, L., Tridon, F., and Planche, C.: Investigating secondary ice production in a deep convective cloud with a 3D bin microphysics model: Part I - Sensitivity study of microphysical processes representations, *Atmospheric Research*, 313, 107 774, <https://doi.org/10.1016/j.atmosres.2024.107774>, 2025.
- Hallet, J. and Mossop, S. C.: Production of secondary ice particles during the riming process, *Nature*, 249, 26–28, <https://doi.org/10.1038/249026a0>, 1974.
- 135 Heymsfield, A., Lawson, P., and DeMott, P.: SPICULE | Earth Observing Laboratory, https://www.eol.ucar.edu/field_projects/spicule, 2024.
- Lawson, R. P., Woods, S., and Morrison, H.: The Microphysics of Ice and Precipitation Development in Tropical Cumulus Clouds, *Journal of the Atmospheric Sciences*, 72, 2429–2445, <https://doi.org/10.1175/JAS-D-14-0274.1>, 2015.
- Lawson, R. P., Korolev, A. V., DeMott, P. J., Heymsfield, A. J., Brientjes, R. T., Wolff, C. A., Woods, S., Patnaude, R. J., Jensen, J. B., 140 Moore, K. A., Heckman, I., Rosky, E., Haggerty, J., Perkins, R. J., Fisher, T., and Hill, T. C. J.: The Secondary Production of Ice in

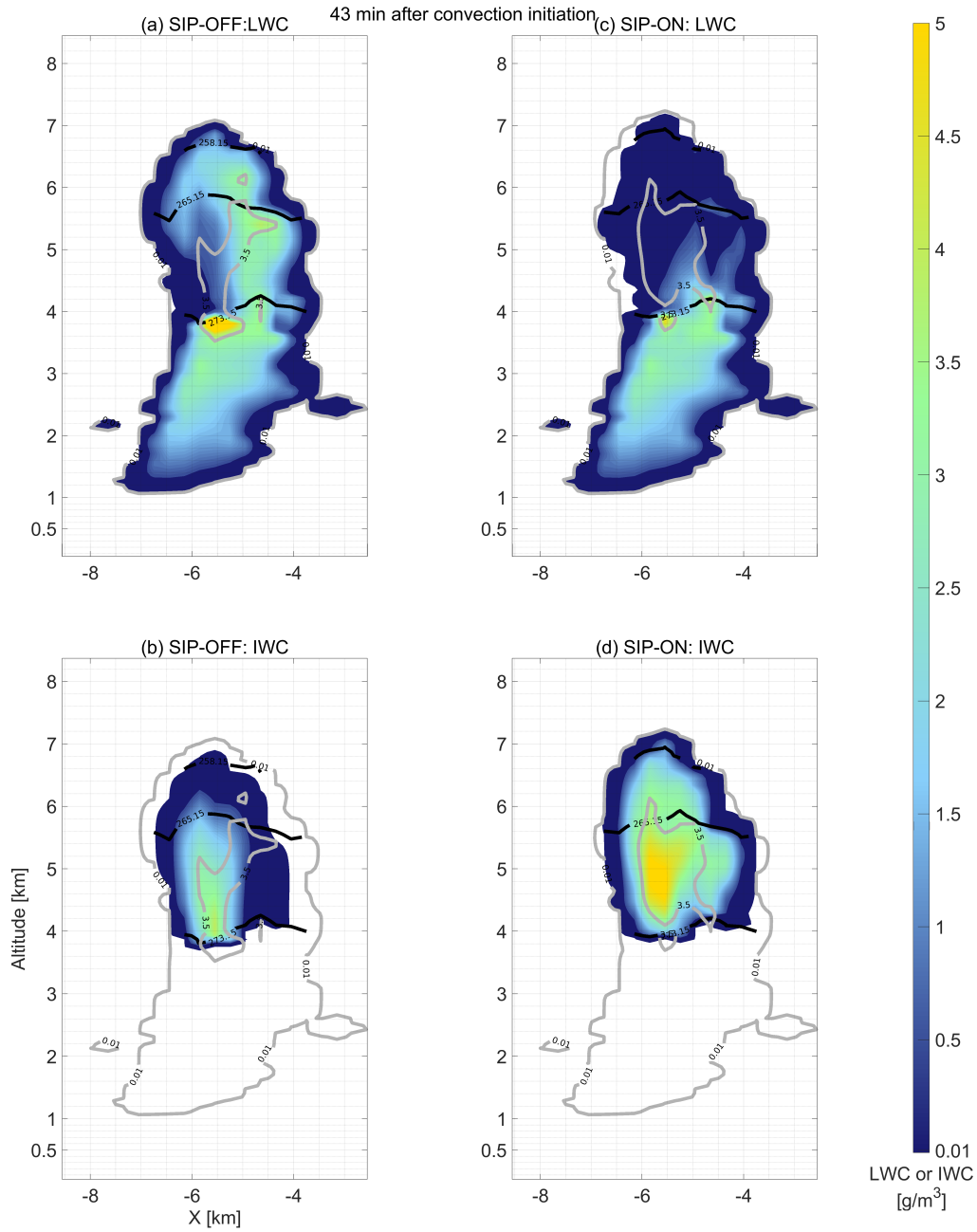


Figure S9. Vertical profile of liquid water content (LWC) and ice water content (IWC) at 43 min after convection initiation. Contour lines in gray indicate Total Water Content (TWC) values of 0.01 gm^{-3} and 3.5 gm^{-3} to enclose cloudy and core conditions. Continuous black lines indicate altitudes at which temperatures are 273.15 K, 265.15 K and 258.15 K corresponding to freezing, maximum ice multiplication by rime splintering and by droplet shattering, respectively. Panels (a-b) Simulation scenario without secondary ice processes. Panel (c-d) Simulation scenario with secondary ice processes including rime splintering (RS) (Hallet and Mossop, 1974), droplet shattering (DS) (Phillips et al., 2018) and ice-ice collisional breakup (IIBR) (Phillips et al., 2017; Grzegorzczek et al., 2025)

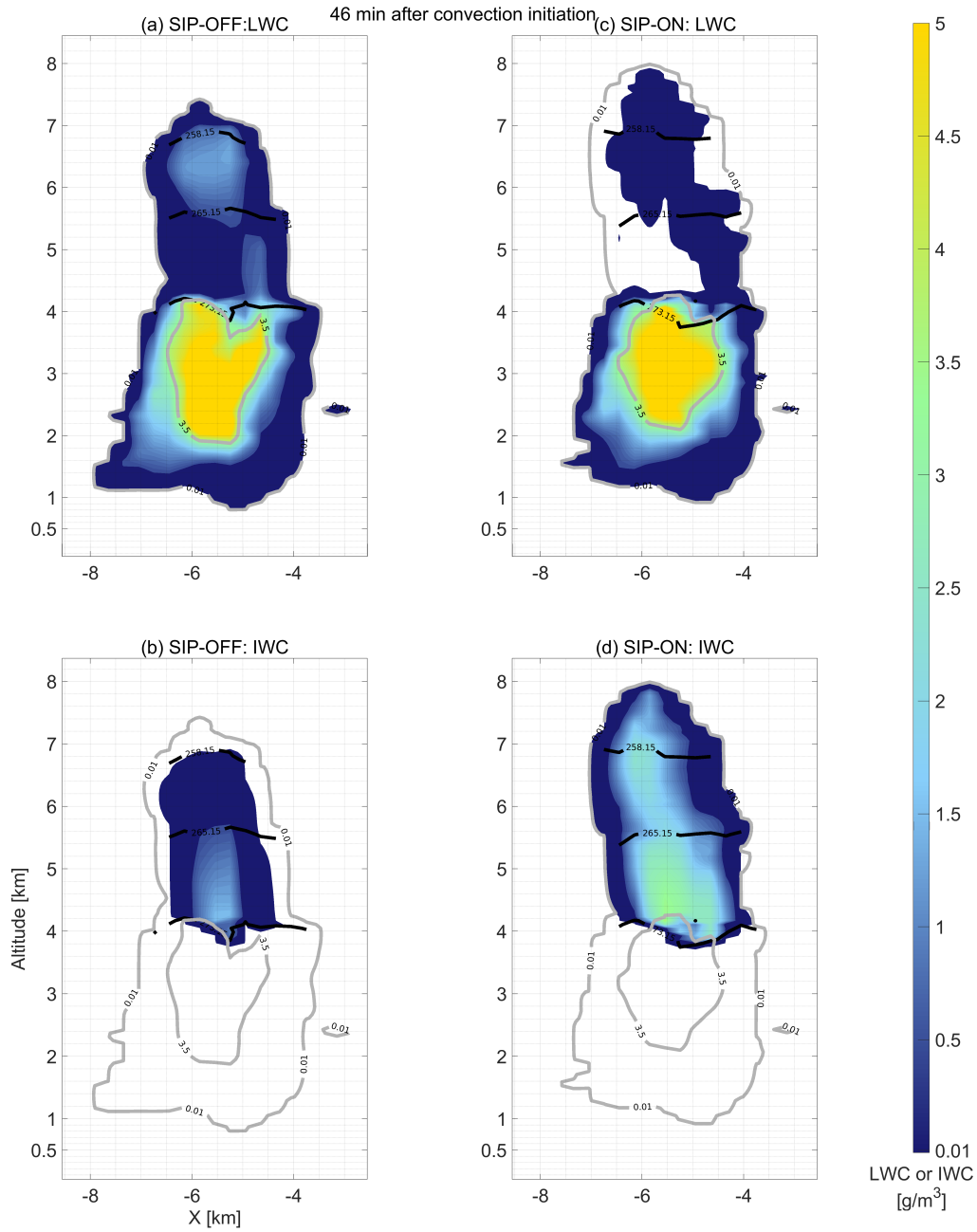


Figure S10. Vertical profile of liquid water content (LWC) and ice water content (IWC) at 46 min after convection initiation. Contour lines in gray indicate Total Water Content (TWC) values of 0.01 g m^{-3} and 3.5 g m^{-3} to enclose cloudy and core conditions. Continuous black lines indicate altitudes at which temperatures are 273.15 K, 265.15 K and 258.15 K corresponding to freezing, maximum ice multiplication by rime splintering and by droplet shattering, respectively. Panels (a-b) Simulation scenario without secondary ice processes. Panel (c-d) Simulation scenario with secondary ice processes including rime splintering (RS) (Hallet and Mossop, 1974), droplet shattering (DS) (Phillips et al., 2018) and ice-ice collisional breakup (IIBR) (Phillips et al., 2017; Grzegorzczuk et al., 2025)

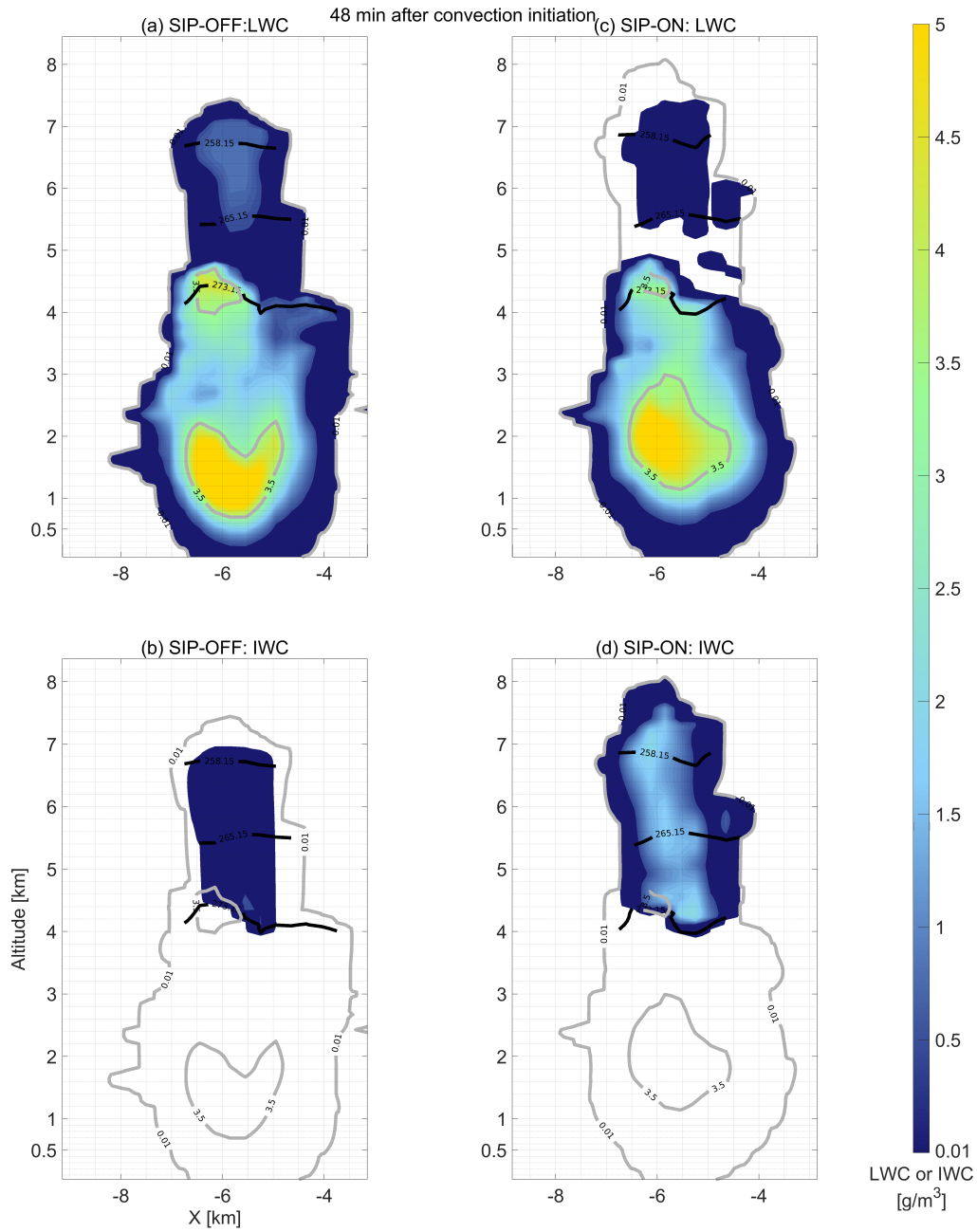


Figure S11. Vertical profile of liquid water content (LWC) and ice water content (IWC) at 48 min after convection initiation. Contour lines in gray indicate Total Water Content (TWC) values of 0.01 g m^{-3} and 3.5 g m^{-3} to enclose cloudy and core conditions. Continuous black lines indicate altitudes at which temperatures are 273.15 K, 265.15 K and 258.15 K corresponding to freezing, maximum ice multiplication by rime splintering and by droplet shattering, respectively. Panels (a-b) Simulation scenario without secondary ice processes. Panel (c-d) Simulation scenario with secondary ice processes including rime splintering (RS), droplet shattering (DS) and ice-ice collisional breakup (IIBR)

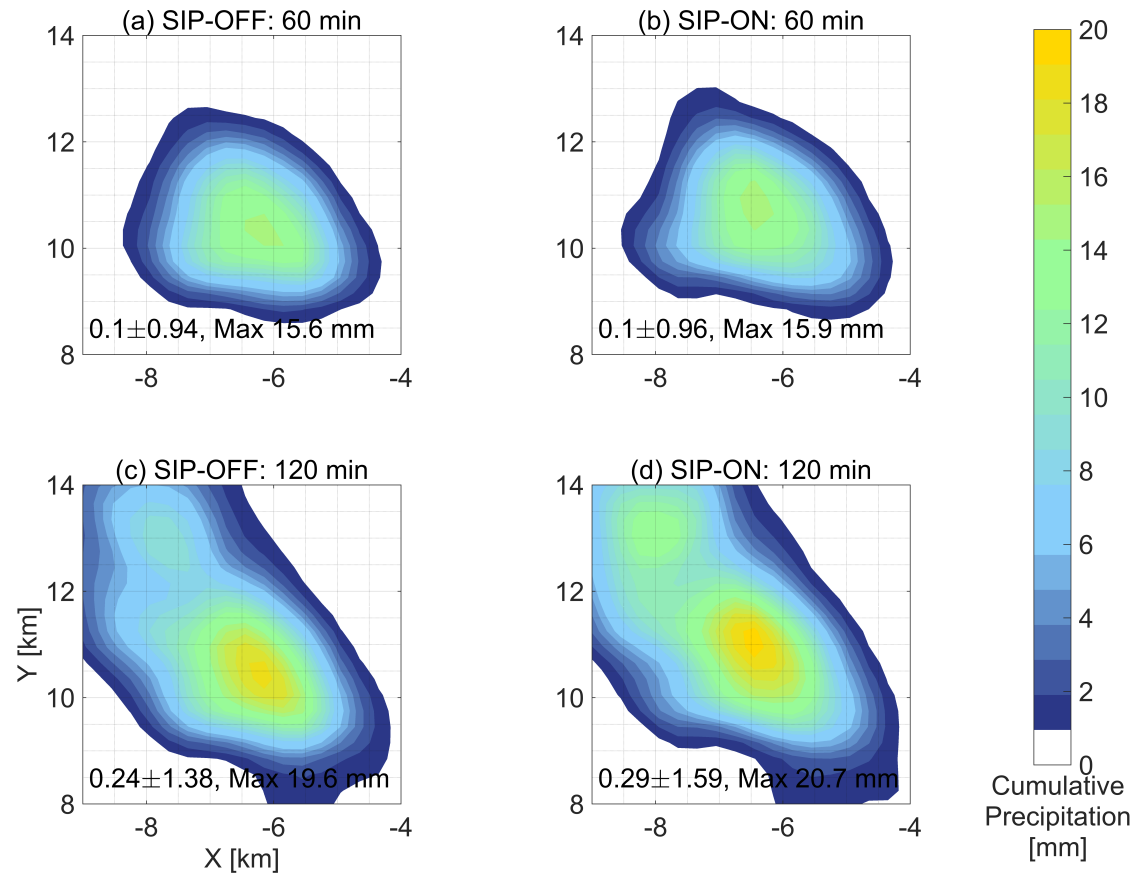


Figure S12. Cumulative precipitation at surface level at the time instances of 60 min and 120 min after convection initiation in the simulation scenarios of panels (a,c) Simulation scenario without secondary ice processes, panels (b,d) Simulation scenario secondary ice processes including rime splintering (RS), droplet shattering (DS) and ice–ice collisional breakup (IIBR)

- Cumulus Experiment (SPICULE), Bulletin of the American Meteorological Society, 104, E51 – E76, <https://doi.org/10.1175/BAMS-D-21-0209.1>, 2023.
- Leisner, T., Pander, T., Handmann, T., and Kiselev, A.: Secondary ice processes upon heterogeneous freezing of cloud droplets, in: Proceedings of the 14th Conference on Cloud Physics and Atmospheric Radiation, American Meteorological Society, <https://ams.confex.com/ams/14CLOUD14ATRAD/webprogram/Paper250221.html>, 2014.
- Mossop, S. C.: Production of secondary ice particles during the growth of graupel by riming, Quarterly Journal of the Royal Meteorological Society, 102, 45–57, <https://doi.org/10.1002/qj.49710243104>, 1976.
- Phillips, V. T. J., Yano, J.-I., and Khain, A.: Ice Multiplication by Breakup in Ice–Ice Collisions. Part I: Theoretical Formulation, Journal of the Atmospheric Sciences, 74, 1705–1719, <https://doi.org/10.1175/JAS-D-16-0224.1>, 2017.
- Phillips, V. T. J., Patade, S., Gutierrez, J., and Bansemer, A.: Secondary Ice Production by Fragmentation of Freezing Drops: Formulation and Theory, Journal of the Atmospheric Sciences, 75, 3031–3070, <https://doi.org/10.1175/JAS-D-17-0190.1>, 2018.
- Savre, J., Ekman, A. M. L., and Svensson, G.: Technical note: Introduction to MIMICA, a large-eddy simulation solver for cloudy planetary boundary layers, Journal of Advances in Modeling Earth Systems, 6, 630–649, <https://doi.org/10.1002/2013MS000292>, 2014.
- Sotiropoulou, G., Vignon, E., Young, G., Morrison, H., O’Shea, S. J., Lachlan-Cope, T., Berne, A., and Nenes, A.: Secondary ice production in summer clouds over the Antarctic coast: an underappreciated process in atmospheric models, Atmospheric Chemistry and Physics, 21, 755–771, <https://doi.org/10.5194/acp-21-755-2021>, 2021.

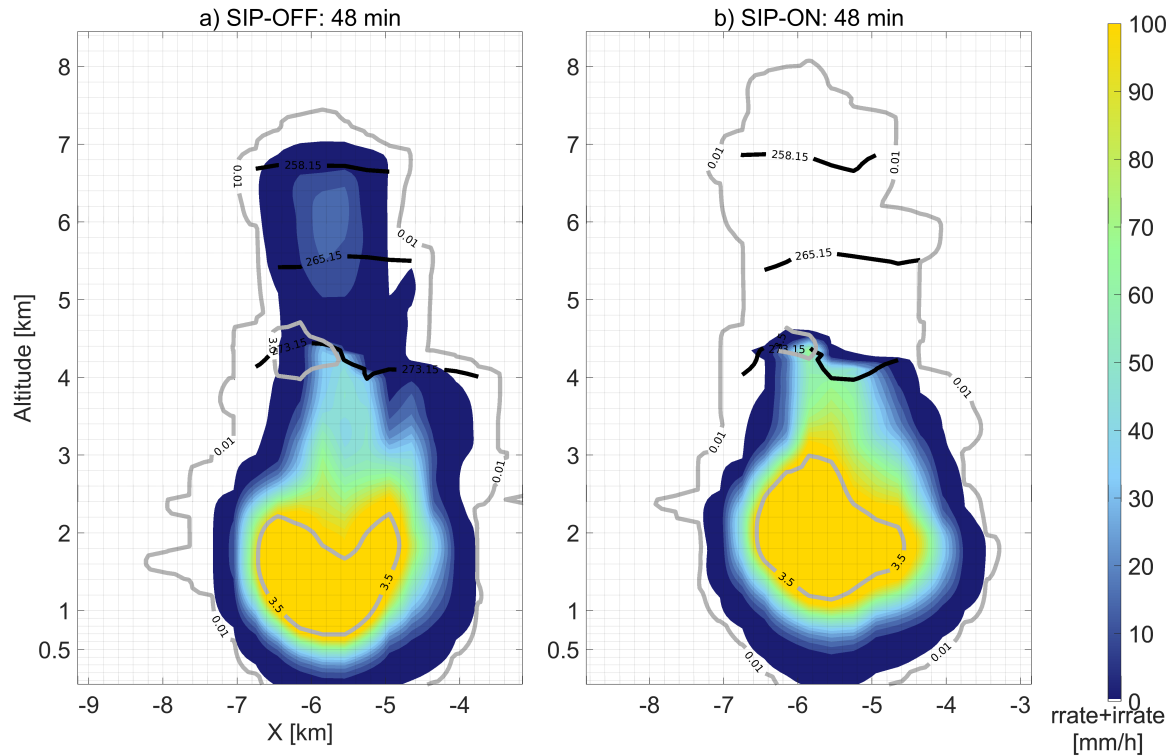


Figure S13. Vertical profile of liquid and ice precipitation rates expressed as $\text{rrate} + \text{irate}$ at 48 min after convection initiation. Continuous gray lines indicate limits of cloudy conditions. Contour lines indicate updrafts (red) and downdrafts (blue). Continuous black lines indicate altitudes at which temperatures are 273.15 K, 265.15 K and 258.15 K corresponding to freezing, maximum ice multiplication by rime splintering and by droplet shattering, respectively. Panel a) Simulation scenario without secondary ice processes. Panel b) Simulation scenario with secondary ice processes including rime splintering (RS), droplet shattering (DS) and ice-ice collisional breakup (IIBR)

Sullivan, S. C., Hoose, C., and Nenes, A.: Investigating the contribution of secondary ice production to in-cloud ice crystal numbers, *Journal of Geophysical Research: Atmospheres*, 122, 9391–9412, <https://doi.org/10.1002/2017JD026546>, 2017.

160 Sullivan, S. C., Hoose, C., Kiselev, A., Leisner, T., and Nenes, A.: Initiation of secondary ice production in clouds, *Atmospheric Chemistry and Physics*, 18, 1593–1610, <https://doi.org/10.5194/acp-18-1593-2018>, 2018.

Takahashi, T., Nagao, Y., and Kushiya, Y.: Possible High Ice Particle Production during Graupel–Graupel Collisions, *Journal of Atmospheric Sciences*, 52, 4523–4527, [https://doi.org/10.1175/1520-0469\(1995\)052<4523:PHIPPD>2.0.CO;2](https://doi.org/10.1175/1520-0469(1995)052<4523:PHIPPD>2.0.CO;2), 1995.

165 Tonttila, J., Afzalifar, A., Kokkola, H., Raatikainen, T., Korhonen, H., and Romakkaniemi, S.: Precipitation enhancement in stratocumulus clouds through airborne seeding: sensitivity analysis by UCLALES-SALSA, *Atmospheric Chemistry and Physics*, 21, 1035–1048, <https://doi.org/10.5194/acp-21-1035-2021>, 2021.

UCAR/NCAR - Earth Observing Laboratory: SPICULE: Flight Tracks - Google Earth .kml files. Version 1.0, <https://doi.org/10.26023/MZCA-XP1F-DC12>, accessed 09 Jun 2025, 2021.

170 Ziegler, C. L., Ray, P. S., and MacGorman, D. R.: Relations of Kinematics, Microphysics and Electrification in an Isolated Mountain Thunderstorm, *Journal of Atmospheric Sciences*, 43, 2098 – 2115, [https://doi.org/10.1175/1520-0469\(1986\)043<2098:ROKMAE>2.0.CO;2](https://doi.org/10.1175/1520-0469(1986)043<2098:ROKMAE>2.0.CO;2), 1986.

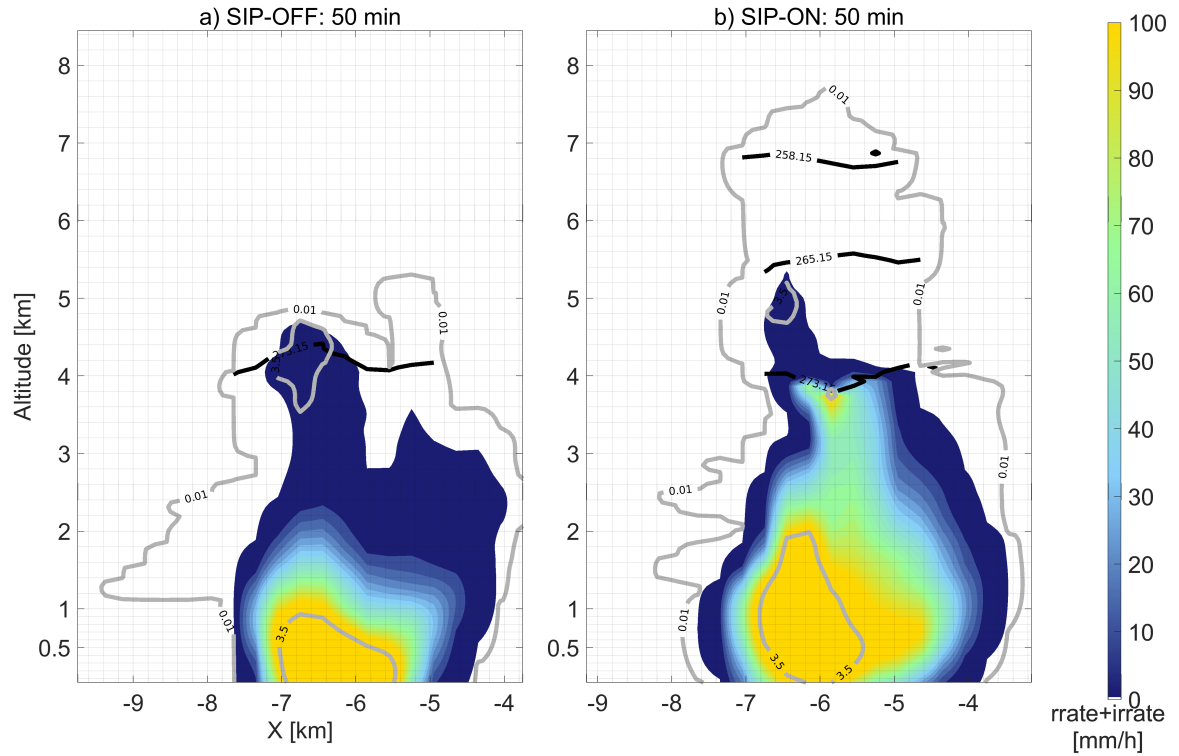


Figure S14. Vertical profile of liquid and ice precipitation rates expressed as $rrate+irate$ at 50 min after convection initiation. Continuous gray lines indicate limits of cloudy conditions. Contour lines indicate updrafts (red) and downdrafts (blue). Continuous black lines indicate altitudes at which temperatures are 273.15 K, 265.15 K and 258.15 K corresponding to freezing, maximum ice multiplication by rime splintering and by droplet shattering, respectively. Panel a) Simulation scenario without secondary ice processes. Panel b) Simulation scenario secondary ice processes including rime splintering (RS), droplet shattering (DS) and ice-ice collisional breakup (IIBR)